
Accelerating Visual-Policy Learning through Parallel Differentiable Simulation

Haoxiang You
Department of Mechanical Engineering
Yale University
New Haven, CT 06520
haoxiang.you@yale.edu

Yilang Liu
Department of Mechanical Engineering
Yale University
New Haven, CT 06520
yilang.liu@yale.edu

Ian Abraham
Department of Mechanical Engineering
Yale University
New Haven, CT 06520
ian.abraham@yale.edu

Abstract

In this work, we propose a computationally efficient algorithm for visual policy learning that leverages differentiable simulation and first-order analytical policy gradients. Our approach decouples the rendering process from the computation graph, enabling seamless integration with existing differentiable simulation ecosystems without the need for specialized differentiable rendering software. This decoupling not only reduces computational and memory overhead but also effectively attenuates the policy gradient norm, leading to more stable and smoother optimization. We evaluate our method on standard visual control benchmarks using modern GPU-accelerated simulation. Experiments show that our approach significantly reduces wall-clock training time and consistently outperforms all baseline methods in terms of final returns. Notably, on complex tasks such as humanoid locomotion, our method achieves a $4\times$ improvement in final return, and successfully learns a humanoid running policy within 4 hours on a single GPU. Videos and code are available on https://haoxiangyou.github.io/Dva_website/

1 Introduction

Learning to control robots from visual inputs is a key challenge in robotics, with the potential to enable a wide range of real-world applications, ranging from autonomous driving and home service robots to industrial automation. Most methods for learning visual policies fall into two categories: imitation learning and reinforcement learning (RL). Imitation learning trains policies by mimicking expert demonstrations, which are typically collected via human operation [Bojarski et al., 2016, Kendall et al., 2019] or teleoperation systems [Chi et al., 2024, Black et al., 2024]. When expert demonstrations are scarce or difficult to obtain, visual policies can instead be learned through RL [Mnih et al., 2015, Hafner et al., 2019]. However, RL methods typically require long training times and substantial computational resources, such as large-scale GPU clusters, to achieve effective control.

Recent advances in differentiable simulation have enabled alternative policy optimization methods, known as analytical policy gradients (APG) [Freeman et al., 2021, Xu et al., 2021, Schwarke et al., 2024]. These methods achieve much higher computational efficiency by replacing zeroth-order gradient estimates with first-order gradients. However, extending APG methods to visual control



Figure 1: **Fast training of humanoid running policy from pixel input.** Our method learns a stable running gait in 4 hours on a single RTX 4080 GPU.

remains challenging: obtaining high-quality differentiable rendering is non-trivial, and computing Jacobians over pixel inputs is both memory- and computationally inefficient. Consequently, existing approaches either train separate differentiable renderers [Wiedemann et al., 2023, Liu et al., 2024] or rely on low-dimensional visual features, which demand considerable engineering effort [Heeg et al., 2024, Luo et al., 2024].

In this work, we propose Decoupled Visual-Based Analytical Policy Gradient (D.Va), a novel method for learning visual policies using differentiable simulation. The core idea is to decouple visual observations from the computation graph, eliminating the need to differentiate through the rendering process. We find that this decoupling not only improves memory and computational efficiency by avoiding Jacobian computations over pixel space, but also normalizes the policy gradient, making visual policy learning more stable. We further provide a formal analysis of our new computation graph, demonstrating that the proposed decoupling policy gradient can be interpreted as a form of policy distillation from open-loop trajectory optimization. This reveals a fundamental connection between open-loop trajectory optimization and closed-loop policy learning.

Finally, we benchmark a diverse set of visual policy learning methods using a GPU-accelerated simulation platform that supports parallelized physics and rendering, providing a robust and scalable testbed for evaluation. Our comparisons include the proposed D.Va, two model-free RL algorithms [Laskin et al., 2020a, Yarats et al., 2021], the model-based RL method DreamerV3 [Hafner et al., 2023], an analytical policy gradient method with differentiable rendering, and state-to-visual distillation [Mu et al., 2025]—a two-stage framework that first trains a state-based policy and then distills it into a visual policy through imitation learning. Experiments highlight D.Va’s superior computational efficiency across a wide range of control tasks.

In summary, our contributions are: (a) Proposing D.Va, a computationally efficient method for visual policy learning; (b) Benchmarking diverse visual policy learning approaches on state-of-the-art simulation platforms; (c) Providing an analysis of analytical policy gradients and highlighting the new opportunities for integrating policy learning with trajectory optimization techniques.

2 Background

In this section, we formally define the policy optimization problem and introduce key concepts in analytical policy gradient methods.

2.1 Problem formulation

We consider the dynamical system $\mathbf{s}_{t+1} = f(\mathbf{s}_t, \mathbf{a}_t)$, where $\mathbf{s}_t \in \mathcal{S}$ denotes the state and $\mathbf{a}_t \in \mathcal{A}$ the action. The dynamics function $f : \mathcal{S} \times \mathcal{A} \rightarrow \mathcal{S}$ is assumed to be fully differentiable with respect to both state and action. Let $\mathbf{o}_t = g(\mathbf{s}_t) \in \mathcal{O}$ denote the observation, where $g : \mathcal{S} \rightarrow \mathcal{O}$ is the sensor model. Throughout this paper, we assume \mathbf{s}_t is a low-dimensional internal representation of the robot (e.g., joint states), while \mathbf{o}_t represents observation derived from \mathbf{s}_t (e.g., images).

Consider the trajectory $\tau = \{\mathbf{s}_0, \mathbf{a}_0, \mathbf{s}_1, \mathbf{a}_1, \dots, \mathbf{s}_T, \mathbf{a}_T\}$, which is a sequence of state-action pairs with horizon T . The total return is defined as $\mathcal{J}(\tau) = \sum_{i=0}^T \gamma^i R(\mathbf{s}_i, \mathbf{a}_i)$, where $\gamma \in (0, 1)$ is the discount factor, and $R : \mathcal{S} \times \mathcal{A} \rightarrow \mathbb{R}$ is the reward function. We denote the discounted temporal reward as $r_t = \gamma^t R(\mathbf{s}_t, \mathbf{a}_t)$. A feedback policy $\pi(\cdot | \mathbf{o}_t, \boldsymbol{\theta}) : \mathcal{O} \times \Theta \rightarrow \Delta(\mathcal{A})$ is a family of conditional probability distributions that maps an observation to a probability distribution over actions. Typically, this distribution is modeled as a Gaussian, allowing the action to be expressed via

the reparameterization trick: $\mathbf{a}_t = \boldsymbol{\mu}(\mathbf{o}_t, \boldsymbol{\theta}) + \boldsymbol{\sigma}(\mathbf{o}_t, \boldsymbol{\theta}) \odot \boldsymbol{\epsilon}_t$ where $\boldsymbol{\mu} : \mathcal{O} \times \Theta \rightarrow \mathcal{A}$, $\boldsymbol{\sigma} : \mathcal{O} \times \Theta \rightarrow \mathcal{A}$ represent the mean and standard deviation respectively, and $\boldsymbol{\epsilon}_t \sim \mathcal{N}(\mathbf{0}, \mathbf{I})$ is injected noise. Given an initial condition \mathbf{s}_0 , and a sequence of injected noises $\mathcal{E} = \{\boldsymbol{\epsilon}_0, \boldsymbol{\epsilon}_1, \dots, \boldsymbol{\epsilon}_T\}$, a trajectory τ can be generated by rolling out from policy under dynamics f and sensor model g , which we explicitly denoted as $\tau(\mathbf{s}_0, \boldsymbol{\theta}, \mathcal{E})$ and the corresponding return as $\mathcal{J}(\tau(\mathbf{s}_0, \boldsymbol{\theta}, \mathcal{E}))$. For notational simplicity, we omit the explicit trajectory τ and write the return directly as $\mathcal{J}(\mathbf{s}_0, \boldsymbol{\theta}, \mathcal{E})$. The expected return for a given policy is defined as $\mathcal{V}(\boldsymbol{\theta}) = \mathbb{E}_{\mathbf{s}_0 \sim \rho_0} \mathbb{E}_{\boldsymbol{\epsilon}_t \sim \mathcal{N}(\mathbf{0}, \mathbf{I})} \mathcal{J}(\mathbf{s}_0, \boldsymbol{\theta}, \mathcal{E})$, where ρ_0 is initial distribution. The goal of policy optimization is to find policy parameters $\boldsymbol{\theta}$ maximizing the expected return.

2.2 Analytical policy gradient

Here, we provide background on analytical policy gradient (APG) methods. These methods compute the policy gradient as

$$\nabla_{\boldsymbol{\theta}} \mathcal{V} = \mathbb{E}_{\mathbf{s}_0 \sim \rho_0} \mathbb{E}_{\boldsymbol{\epsilon}_t \sim \mathcal{N}(\mathbf{0}, \mathbf{I})} \nabla_{\boldsymbol{\theta}} \mathcal{J}(\mathbf{s}_0, \boldsymbol{\theta}, \mathcal{E}) = \mathbb{E}_{\mathbf{s}_0 \sim \rho_0} \mathbb{E}_{\boldsymbol{\epsilon}_t \sim \mathcal{N}(\mathbf{0}, \mathbf{I})} \left[\sum_{t=0}^T \nabla_{\boldsymbol{\theta}} r_t \right], \quad (1)$$

where the gradient of each term in the sum is given by

$$\begin{aligned} \nabla_{\boldsymbol{\theta}} r_t &= \frac{\partial r_t}{\partial \mathbf{a}_t} \frac{d\mathbf{a}_t}{d\boldsymbol{\theta}} + \frac{\partial r_t}{\partial \mathbf{s}_t} \frac{d\mathbf{s}_t}{d\boldsymbol{\theta}}, \quad t = 0, \dots, T \\ \frac{d\mathbf{a}_t}{d\boldsymbol{\theta}} &= \frac{\partial \mathbf{a}_t}{\partial \boldsymbol{\theta}} + \frac{\partial \mathbf{a}_t}{\partial \mathbf{o}_t} \frac{d\mathbf{o}_t}{d\mathbf{s}_t} \frac{d\mathbf{s}_t}{d\boldsymbol{\theta}}, \quad t = 0, \dots, T \\ \frac{d\mathbf{s}_t}{d\boldsymbol{\theta}} &= \frac{\partial \mathbf{s}_t}{\partial \mathbf{s}_{t-1}} \frac{d\mathbf{s}_{t-1}}{d\boldsymbol{\theta}} + \frac{\partial \mathbf{s}_t}{\partial \mathbf{a}_{t-1}} \frac{d\mathbf{a}_{t-1}}{d\boldsymbol{\theta}}, \quad t = 1 \dots T \text{ and } \frac{d\mathbf{s}_0}{d\boldsymbol{\theta}} = \mathbf{0}. \end{aligned} \quad (2)$$

Here, $\frac{d}{d\boldsymbol{\theta}}$ denotes the total derivative, and $\frac{\partial}{\partial}$ represents the partial derivative, both expressed in matrix form as Jacobians. The expectation can then be estimated via empirical sum. As these methods estimate the first-order policy gradient by backpropagation through trajectories, they are also named as first-order policy gradients (FoPG) or backpropagation through time (BPTT).

Short-horizon actor critic (SHAC) The trajectory gradient, i.e., $\nabla_{\boldsymbol{\theta}} \mathcal{J}(\mathbf{s}_0, \boldsymbol{\theta}, \mathcal{E})$, can quickly become intractable as the horizon T increases due to exploding gradients by multiplying a series of matrices. The exploding gradient of an individual trajectory leads to the high-variance empirical estimate of the policy gradient [Metz et al., 2021], as well as an empirical bias problem [Suh et al., 2022]. Fortunately, these problems are largely solved by the Short-Horizon Actor-Critic (SHAC) method [Xu et al., 2021]. The key idea is to truncate the long trajectory into smaller segments and incorporate a learned value function for long-horizon predictions. More specifically, at each iteration, the SHAC algorithm optimizes the following actor loss

$$\mathcal{L}_{\boldsymbol{\theta}} = -\frac{1}{Nh} \sum_{i=1}^N \left[\left(\sum_{t=t_0}^{t_0+h-1} \gamma^{t-t_0} R(\mathbf{s}_t^{(i)}, \mathbf{a}_t^{(i)}) \right) + \gamma^h V_{\phi}(\mathbf{s}_{t_0+h}^{(i)}) \right], \quad (3)$$

where $\mathbf{s}_t^{(i)}$ and $\mathbf{a}_t^{(i)}$ are states and actions of the i -th trajectory rollout, and $V_{\phi} : \mathcal{S} \rightarrow \mathbb{R}$ is the value function learned with TD- λ tricks [Sutton et al., 1998].

3 Method

In this work, we extend SHAC to handle complex observations, e.g., images, whereas the original SHAC primarily focused on low-dimensional state spaces. The main challenge in visual setting is calculating the observation Jacobian $\frac{d\mathbf{o}_t}{d\mathbf{s}_t}$, which is both computationally and memory intensive due to the high dimensionality of images. To address this, we omit all terms of the form $\left(\frac{\partial \mathbf{a}_t}{\partial \mathbf{o}_t} \frac{d\mathbf{o}_t}{d\mathbf{s}_t} \frac{d\mathbf{s}_t}{d\boldsymbol{\theta}} \right)$, resulting in a quasi-policy gradient that we refer to as the decoupled policy gradient (DPG). In this section, we provide a formal analysis showing how the DPG works, as well as algorithm that utilizes DPG for training a visual policy.

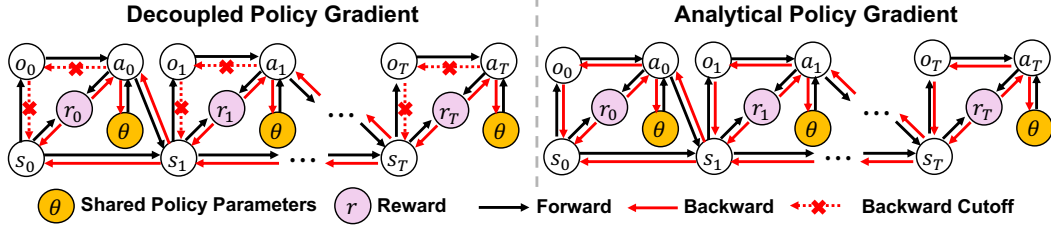


Figure 2: **Computation graphs of decoupled policy gradient (DPG) and APG.** The policy gradient is traced from any reward r_t , propagated backward through the graph to the shared parameters θ . APG backpropagates through the entire pipeline, whereas the DPG prevents gradient flow through the rendering process.

3.1 Decoupled policy gradient

We divide the analytical policy gradient (1) into two parts by separating all terms involving $\frac{d\mathbf{o}_t}{ds_t}$ from those that do not: $\nabla_{\theta}\mathcal{V} = \tilde{\nabla}_{\theta}\mathcal{V} + \mathcal{B}$, where

$$\begin{aligned}\tilde{\nabla}_{\theta}\mathcal{V} &= \mathbb{E}_{\mathbf{s}_0 \sim \rho_0} \mathbb{E}_{\epsilon_t \sim \text{i.i.d. } \mathcal{N}(\mathbf{0}, \mathbf{I})} \left[\tilde{\nabla}_{\theta} \mathcal{J}(\mathbf{s}_0, \theta, \mathcal{E}) \right] = \mathbb{E}_{\mathbf{s}_0 \sim \rho_0} \mathbb{E}_{\epsilon_t \sim \text{i.i.d. } \mathcal{N}(\mathbf{0}, \mathbf{I})} \left[\sum_{t=0}^T \tilde{\nabla}_{\theta} r_t \right] \\ \tilde{\nabla}_{\theta} r_t &= \frac{\partial r_t}{\partial \mathbf{a}_t} \frac{\partial \mathbf{a}_t}{\partial \theta} + \frac{\partial r_t}{\partial \mathbf{s}_t} \frac{d\tilde{\mathbf{s}}_t}{d\theta}, \quad t = 0 \dots T \\ \frac{d\tilde{\mathbf{s}}_t}{d\theta} &= \frac{\partial \mathbf{s}_t}{\partial \mathbf{s}_{t-1}} \frac{d\tilde{\mathbf{s}}_{t-1}}{d\theta} + \frac{\partial \mathbf{s}_t}{\partial \mathbf{a}_{t-1}} \frac{\partial \mathbf{a}_{t-1}}{\partial \theta}, \quad t = 1 \dots T \quad \text{and} \quad \frac{d\tilde{\mathbf{s}}_0}{d\theta} = \mathbf{0},\end{aligned}\quad (4)$$

and

$$\begin{aligned}\mathcal{B} &= \mathbb{E}_{\mathbf{s}_0 \sim \rho_0} \mathbb{E}_{\epsilon_t \sim \text{i.i.d. } \mathcal{N}(\mathbf{0}, \mathbf{I})} \left[\sum_{t=0}^T \left(\frac{\partial r_t}{\partial \mathbf{a}_t} \frac{\partial \mathbf{a}_t}{\partial \mathbf{o}_t} \frac{d\mathbf{o}_t}{ds_t} \frac{ds_t}{d\theta} \right) \right] \\ \frac{ds_t}{d\theta} &= \frac{\partial \mathbf{s}_t}{\partial \mathbf{a}_{t-1}} \left(\frac{\partial \mathbf{a}_{t-1}}{\partial \theta} + \frac{\partial \mathbf{a}_{t-1}}{\partial \mathbf{o}_{t-1}} \frac{d\mathbf{o}_{t-1}}{ds_{t-1}} \frac{ds_{t-1}}{d\theta} \right) + \frac{\partial \mathbf{s}_t}{\partial \mathbf{s}_{t-1}} \frac{ds_{t-1}}{d\theta}, \quad t = 1 \dots T \quad \text{and} \quad \frac{ds_0}{d\theta} = \mathbf{0}.\end{aligned}\quad (5)$$

Detailed derivation of this decomposition is provided in Appendix A. We refer to $\tilde{\nabla}_{\theta}\mathcal{V}$ (4) as the *decoupled policy gradient*, which improves the policy by distilling results from open-loop trajectory optimizations. We denote \mathcal{B} (5) as *control regularization* which captures the interdependence between actions. Below, we provide a conceptual explanation of each term, describe the rationale behind their naming, and validate the effectiveness of the decoupled policy gradient through experiments.

Distilling from open-loop Trajectories Here, we show how the decoupled policy gradient (4) can be interpreted as distilling from open-loop trajectories. We begin by initializing an open-loop sequence of controls, $\mathbf{A} = \{\mathbf{a}_0, \mathbf{a}_1, \dots, \mathbf{a}_T\}$, by rolling out the policy $\pi(\cdot; \theta)$ under the initial condition \mathbf{s}_0 . Given the open-loop control sequence \mathbf{A} and initial condition \mathbf{s}_0 , the sequence of states $\mathbf{S} = \{\mathbf{s}_0, \mathbf{s}_1, \dots, \mathbf{s}_T\}$ and observation $\mathbf{O} = \{\mathbf{o}_0, \mathbf{o}_1, \dots, \mathbf{o}_T\}$ can be reconstructed via dynamics f and sensor model g . In this case, the return $\mathcal{J}(\mathbf{s}_0, \mathbf{A}) = \sum_{t=0}^T r_t$ is solely a function of the initial condition \mathbf{s}_0 and the control sequence \mathbf{A} . The gradient of return with respect to the control sequence \mathbf{A} is given by

$$\begin{aligned}\nabla_{\mathbf{A}} \mathcal{J} &= \{\nabla_{\mathbf{a}_0} \mathcal{J}, \nabla_{\mathbf{a}_1} \mathcal{J}, \dots, \nabla_{\mathbf{a}_T} \mathcal{J}\}, \quad \text{where} \quad \nabla_{\mathbf{a}_t} \mathcal{J} = \sum_{j=t}^T \nabla_{\mathbf{a}_t} r_j, \quad \text{and} \\ \nabla_{\mathbf{a}_t} r_j &= \begin{cases} \frac{\partial r_j}{\partial \mathbf{s}_j} \frac{\partial \mathbf{s}_j}{\partial \mathbf{s}_{j-1}} \frac{\partial \mathbf{s}_{j-1}}{\partial \mathbf{s}_{j-2}} \dots \frac{\partial \mathbf{s}_{t+2}}{\partial \mathbf{s}_{t+1}} \frac{\partial \mathbf{s}_{t+1}}{\partial \mathbf{a}_t}, & \text{when } j > t \\ \frac{\partial r_t}{\partial \mathbf{a}_t}, & \text{when } j = t \end{cases}, \quad t = 0, \dots, T, \quad j = t, \dots, T.\end{aligned}\quad (6)$$

We improve the control sequence by taking a small step β in the gradient direction for each action

$$\bar{\mathbf{a}}_t = \mathbf{a}_t + \beta \nabla_{\mathbf{a}_t} \mathcal{J}.\quad (7)$$

We denote the updated sequence as $\bar{\mathbf{A}} := \{\bar{\mathbf{a}}_0, \bar{\mathbf{a}}_1, \dots, \bar{\mathbf{a}}_T\}$. The behavior cloning loss is then defined as the discrepancy between the actions generated by the current policy and those in the updated

control sequence:

$$\mathcal{L}_{\text{BC}}(\boldsymbol{\theta}, \mathbf{O}, \bar{\mathbf{A}}, \mathcal{E}) := \frac{1}{2\beta} \sum_{t=0}^T \|\boldsymbol{\mu}(\mathbf{o}_t; \boldsymbol{\theta}) + \boldsymbol{\sigma}(\mathbf{o}_t; \boldsymbol{\theta}) \odot \boldsymbol{\epsilon}_t - \bar{\mathbf{a}}_t\|_2^2, \quad (8)$$

where $\mathcal{E} = \{\boldsymbol{\epsilon}_0, \boldsymbol{\epsilon}_1, \dots, \boldsymbol{\epsilon}_T\}$ is same injected noises use to initialize open-loop sequence \mathbf{A} .

Theorem 1. *The decoupled trajectory gradient in (4) equals the negative gradient of the behavior cloning loss in Equation (8), i.e., $\tilde{\nabla}_{\boldsymbol{\theta}} \mathcal{J}(\mathbf{s}_0, \boldsymbol{\theta}, \mathcal{E}) = -\nabla_{\boldsymbol{\theta}} \mathcal{L}_{\text{BC}}(\boldsymbol{\theta}, \mathbf{O}, \bar{\mathbf{A}}, \mathcal{E})$.*

Proof. Given that the observation sequence \mathbf{O} is generated by rolling out the policy, we have $\mathbf{a}_t = \boldsymbol{\mu}(\mathbf{o}_t; \boldsymbol{\theta}) + \boldsymbol{\sigma}(\mathbf{o}_t; \boldsymbol{\theta}) \odot \boldsymbol{\epsilon}_t$. Therefore, the gradient of the behavior cloning loss simplifies to

$$\nabla_{\boldsymbol{\theta}} \mathcal{L}_{\text{BC}}(\boldsymbol{\theta}, \mathbf{O}, \bar{\mathbf{A}}, \mathcal{E}) = \sum_{t=0}^T \frac{1}{\beta} (\mathbf{a}_t - \bar{\mathbf{a}}_t) \frac{\partial \mathbf{a}_t}{\partial \boldsymbol{\theta}}. \quad (9)$$

Substituting E.q. (7) into 9 resulting in

$$\nabla_{\boldsymbol{\theta}} \mathcal{L}_{\text{BC}}(\boldsymbol{\theta}, \mathbf{O}, \bar{\mathbf{A}}, \mathcal{E}) = \sum_{t=0}^T \frac{1}{\beta} (-\beta \nabla_{\mathbf{a}_t} \mathcal{J}) \frac{\partial \mathbf{a}_t}{\partial \boldsymbol{\theta}} = - \sum_{t=0}^T (\nabla_{\mathbf{a}_t} \mathcal{J}) \frac{\partial \mathbf{a}_t}{\partial \boldsymbol{\theta}}. \quad (10)$$

Finally, substituting $\nabla_{\mathbf{a}_t} \mathcal{J}$ from E.q. (6) into (9) and rearranging terms completes the proof. \square

Theorem 1 highlights the close connection between feedback policy optimization and open-loop trajectory optimization. Iteratively applying gradient ascent with decoupled policy gradient (4) can be interpreted as alternating between two stages: (1) generating trajectories by rolling out the current policy and improving them through trajectory optimization, and (2) distilling the optimized trajectories back into the policy.

Control regularization We now discuss the dropped bias (5), which involves adding multiple terms of the form $\left(\frac{\partial r_t}{\partial \mathbf{a}_t} \frac{\partial \mathbf{a}_t}{\partial \boldsymbol{\theta}} \frac{d\mathbf{o}_t}{ds_t} \frac{ds_t}{d\boldsymbol{\theta}} \right)$. Here, $\frac{\partial r_t}{\partial \mathbf{a}_t}$ captures how the reward at timestep t changes with the action \mathbf{a}_t , while the term $\left(\frac{\partial \mathbf{a}_t}{\partial \boldsymbol{\theta}} \frac{d\mathbf{o}_t}{ds_t} \frac{ds_t}{d\boldsymbol{\theta}} \right)$ reflects how past trajectory influence current decision making, i.e., \mathbf{a}_t . Altogether, the bias term (5) quantifies how the previous experiences influence current actions via coupling through the shared policy, and thereby impacts long-term return. In contrast, the decoupled policy gradient (4) captures how the current action affects future states, but ignores the interdependence between actions.

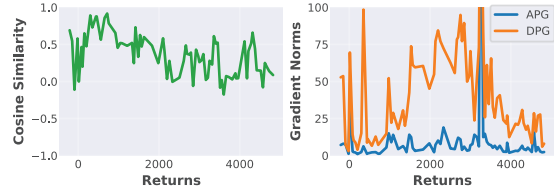


Figure 3: Comparison of APG $\nabla_{\boldsymbol{\theta}} \mathcal{V}$ and DPG $\tilde{\nabla}_{\boldsymbol{\theta}} \mathcal{V}$ on Hopper with full state observation. Both gradients are computed from the same set of $\boldsymbol{\theta}$ values collected during SHAC training. The x-axis shows the return for each $\boldsymbol{\theta}$. **Left:** Cosine similarity is generally positive, indicating $\tilde{\nabla}_{\boldsymbol{\theta}} \mathcal{V}$ is a valid ascent direction. **Right:** Gradient norm between APG and DPG. In this experiment, conducted in state space where $g = \text{identity}$, the control regularization term \mathcal{B} acts as a residual connection. As a result, APG generally exhibits a smaller norm compared to DPG.

Figure 3 compares the APG $\nabla_{\boldsymbol{\theta}} \mathcal{V}$ and DPG $\tilde{\nabla}_{\boldsymbol{\theta}} \mathcal{V}$, both computed with respect to the short-horizon actor loss (3). The cosine similarity between the two gradients is positive in most cases, indicating that $\tilde{\nabla}_{\boldsymbol{\theta}} \mathcal{V}$ generally provides a valid ascent direction for policy improvement. Another noteworthy observation is the difference in norm between the full analytical policy gradient $\nabla_{\boldsymbol{\theta}} \mathcal{V}$ and our quasi-policy-gradient estimate, DPG $\tilde{\nabla}_{\boldsymbol{\theta}} \mathcal{V}$. When we conduct the experiment on state space, i.e., $\mathbf{o}_t = \text{identity}(\mathbf{s}_t) = \mathbf{s}_t$, the additive control regularization (5) operates acts similarly to a residual connection within the computation graph. The additive residual connection contribute to a smoother optimization landscape, making the norm of full APG generally smaller than DPG, as illustrate on Figure 3. This is not the case when the policy is conditioned on high-dimensional visual observations. As we will show shortly in Section 4, when the sensor model g is involving complex rendering process, adding the regularization term \mathcal{B} tends to increase the overall gradient norm, which hinder optimization.

Experimental validation A comparison between full APG and our DPG in full-state space is provided in Appendix D, while results under visual observations are presented in Section 4.

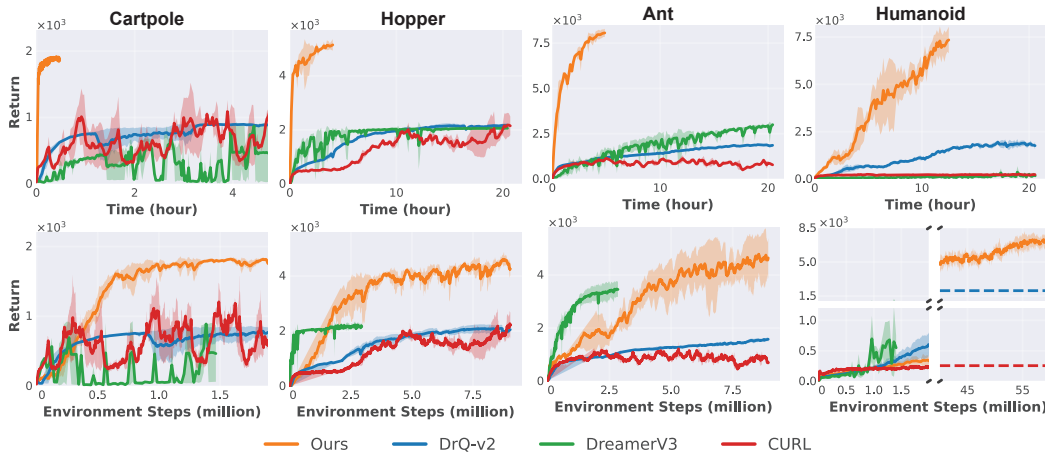


Figure 4: **Comparison with RL: our method achieves substantial speedups and significantly higher rewards across all tasks.** Each curve shows the average performance over five random seeds, with shaded areas indicating standard deviation. In the humanoid task, dashed lines represent the final rewards attained by each algorithm at the end of training. The top row highlights wall-clock efficiency; the bottom row illustrates sample efficiency, with curves truncated at the maximum number of simulation steps for better visualization.

3.2 Decoupled visual based analytical policy gradient

Here, we introduce Decoupled Visual-Based Analytical Policy Gradient (D.Va), a visual policy learning method built upon the decoupled policy gradient formulation. Our method is an on-policy algorithm that updates the policy using parallel simulation to generate short-horizon trajectories. Following SHAC, rollouts resume from previous endpoints and reset at task termination. Trajectories are discarded after each iteration, reducing I/O costs. To capture temporal cues like velocity and acceleration, we stack three consecutive image frames [Hafner et al., 2023, Mu et al., 2025], which are then encoded by a convolutional network to produce a latent vector \mathbf{h}_t for the actor. The critic V_ϕ in Equation (3) plays a crucial role in achieving good overall performance. For efficiency, we train the critic in the low-dimensional state space \mathcal{S} as opposed to the observation space \mathcal{O} . Although the critic is trained using state information, the policy remains state-agnostic throughout the entire training process, enabling direct deployment to downstream tasks without requiring access to privileged state information. Full algorithm details are provided in Appendix B.1.

4 Experiment

We design our experiments to compare the proposed method against common visual policy learning algorithms on GPU-accelerated simulation. Performance is evaluated based on final return, wall-clock time, and the number of environment steps. All hyperparameters are listed in Appendix C, while additional details on setup are provided in the Appendix E.

4.1 Comparison to RL methods

Baseline We compare our method with: (1) DrQ-v2 [Yarats et al., 2021], a model-free method combining image augmentations with DDPG [Lillicrap et al., 2015]; (2) CURL [Laskin et al., 2020a], a model-free RL approach using contrastive learning and SAC [Haarnoja et al., 2018]; and (3) DreamerV3 [Hafner et al., 2023], a model-based algorithm that learns a world model and uses it for planning. All RL baselines are implemented with parallelized simulation to take advantage of faster forward rollout.

Results Our approach achieves comparable sample efficiency to existing methods; however, it excels in wall-clock time and final returns, as shown in Figure 4. The discrepancy between sample and wall-clock time efficiency is because RL methods reuse past experiences through replay buffers, whereas our on-policy method discards samples after each iteration. Consequently, RL methods spend more time updating neural networks—such as fitting Q-functions in DrQ-v2—than collecting new data. As illustrated in Figure 5, only a negligible proportion of time is spent on forward simulation

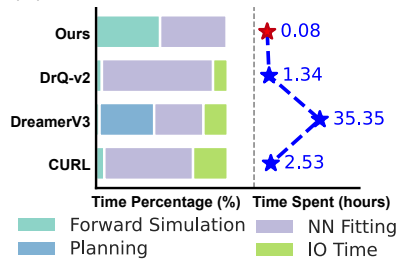


Figure 5: **Training time for Ant over 1M steps.** Left: phase percentages, where “planning” in DreamerV3 refers to rollouts by learned world model. Right: absolute times used per 1M steps. Most time in visual RL is spent fitting neural networks.

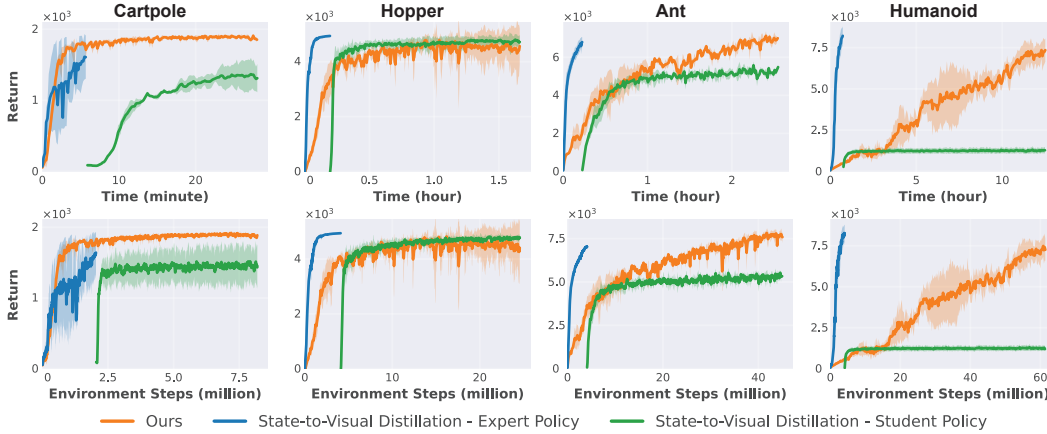


Figure 6: **Compare with State-to-Visual distillation:** Our method matches distilled policy in final return and computation time on three simple tasks, but significantly outperforms it on the more challenging Humanoid locomotion task. The student policy’s x-axis is shifted to account for expert training time. Our implementation builds on Mu et al. [2025], with an enhanced expert training phase by replacing SAC with SHAC.

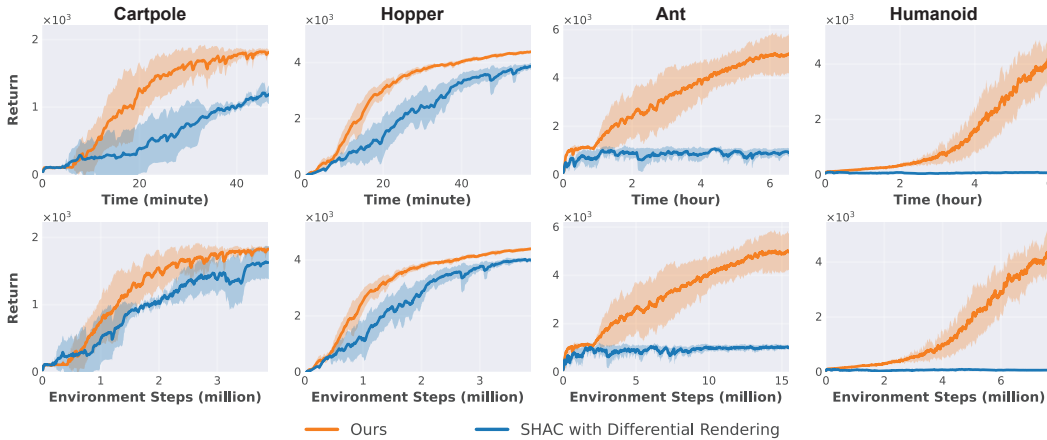


Figure 7: **Compare to SHAC with differential Rendering:** Our method matches SHAC on 2D tasks (Cartpole and Hopper) and outperforms SHAC on more challenging 3D tasks (Ant and Humanoid).

for the RL baselines, indicating limited potential for speedup from faster simulators. In contrast, our method allocates a comparable amount of time to both forward simulation and backward policy updates, suggesting it could further benefit from better simulation.

4.2 Comparison to method using privileged simulation

State-to-visual distillation Another class of popular methods [Loquercio et al., 2021, Chen et al., 2023] training visual policies by first learning an expert policy with privileged state access, then transferring knowledge to a visual policy via Dagger [Ross et al., 2011]. Among these, Mu et al. [2025] proposes two key design choices—early stopping when the behavior cloning loss is low and using off-policy data from a replay buffer, which greatly reduces computation and improves performance. Our implementation of State-to-Visual distillation is based on the approach proposed by Mu et al. [2025], with one key modification: we use SHAC in place of SAC for expert training. We observe that SHAC consistently outperforms model-free SAC in settings where differentiable simulation is available Xu et al. [2021], resulting in further reduced computational time and improved final returns for training State-to-Visual distillation.

Results Our method performs comparably to state-to-visual distillation on three relatively easy tasks in terms of both computation time and final rewards. In these tasks, both approaches achieve returns on par with the expert policy trained in the state space. However, on the more challenging humanoid running task, our method significantly outperforms state-to-visual distillation—achieving high final returns, while distilled policy plateaus at substantially lower values.

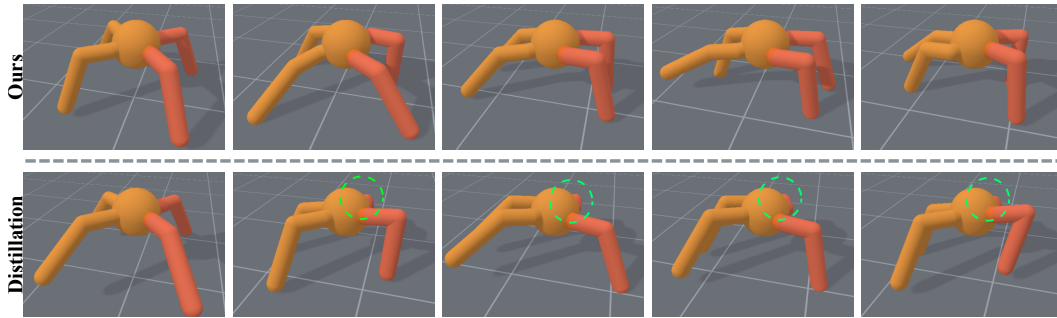


Figure 8: Our method learns policies that are camera-aware, whereas the distilled policy from expert often adopts postures that are partially occluded or blocked from the camera view.

Key difference Here, we highlight the key difference between our method and state-to-vision distillation. While both can be viewed as behavior cloning from another policy, the source of the mimicked policy differs fundamentally. In state-to-visual distillation, actions are imitated from a frozen “expert” policy. In contrast, our method mimics actions from the “teacher” that provides incremental improvements to the current policy. We argue that learning from an incremental “teacher” may be more effective than learning from a fixed “expert”, especially for complex tasks. First, expert actions may differ significantly from those produced by the current policy, making them harder to imitate accurately. Second, expert policy may provide ineffective corrective feedback in those state spaces that are visited by the current policy but rarely seen during its own training phase. In other words, the expert cannot handle situations for which it has no prior experience. We hypothesize that these two factors contribute to the performance gap observed on the humanoid task.

Another subtle but noteworthy difference is in the postures generated by the learned policies. As illustrated in Figure 8, our method consistently produces camera-aware behaviors, while the distilled policy often results in self-occluded postures. Although both the “expert” policy used in distillation and the “teacher” corrections in our method are agnostic to camera views when providing supervision, the on-policy and iterative nature of our approach may lead to important differences. During the student policy distillation phase, imitating actions from unblocked visual inputs may be easier and converge quicker than learning from occluded views, which can introduce ambiguity. Since our method continually discards outdated rollouts and relies on recent data, the training process may be implicitly biased toward favoring trajectories that offer clearer, more informative perspectives.

4.3 Comparison to SHAC with differentiable rendering

Finally, we compare our method against analytical policy gradient approaches that incorporate differentiable rendering. To the best of our knowledge, no existing open-source baseline combines differentiable rendering with analytical policy gradient method; therefore, we provide our own implementation.

We implement differentiable rendering using PyTorch3D [Ravi et al., 2020], in contrast to prior works [Wiedemann et al., 2023, Liu et al., 2024], which rely on a learned renderer. Using a differentiable renderer based on computer graphics eliminates the need to optimize a separate neural network and helps avoid compounding errors from distribution shifts as the scene evolves. Further details on our parallel rendering setup are provided in Appendix B.2. We then train the visual policy end-to-end under the SHAC framework. For a fair comparison, we use identical simulations and neural architectures for both methods, and the value functions are all defined on a low-dimensional state space.

Results Figure 7 compares our method with SHAC across four benchmark problems. We find the performance of SHAC highly dependent on whether the task is 2D or 3D. In the 2D tasks, i.e., Cartpole and Hopper, SHAC achieves performance similar to ours. However, in 3D tasks, our method consistently outperforms SHAC, with SHAC failing to learn effective locomotion. We hypothesize

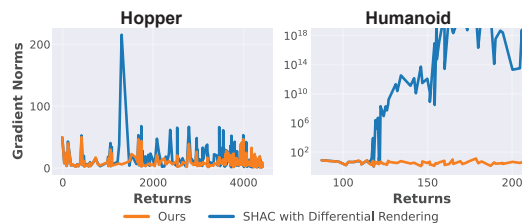


Figure 9: **Comparison of gradient norms between SHAC with differentiable rendering and D.VA:** In this experiment, conducted in the visual space where sensor model g represents a complex rendering process, the control regularization term \mathcal{B} adds to a noisy optimization landscape. As a result, SHAC generally exhibits a larger gradient norm compared to D.VA.

that the discrepancy arises from the noisy optimization landscape introduced by the complex rendering process. In contrast to the low-dimensional state space—where the control regularization term \mathcal{B} (5) acts as a residual connection and the norm of the full APG is generally smaller than that of DPG (see Figure 3)—the high-dimensional visual space involves a more complex sensor model g , which includes 3D transformations and a rasterization process. As a result, the additive control regularization term contributes to a noisier optimization landscape. As shown in Figure 9, the gradient norm of SHAC with differentiable rendering is generally larger than that of our method. Notably, for 3D tasks, the gradient norm in SHAC can rapidly exceed 10^{15} , making the backward signal pure noise. In addition to smoother optimization, several other factors make our method preferable to SHAC for training visual policy in practice. First, our method is significantly more memory efficient, as shown in Figure 10. Second, as scene complexity increases, i.e., the number of meshes and the number of vertices per mesh, SHAC’s memory usage grows rapidly. This is because the Jacobian with respect to each mesh vertex must be stored to construct the computation graph. In contrast, our method avoids storing these large Jacobians, resulting in a relatively stable memory footprint. Therefore, our method is more suitable for tasks involving a greater number of objects and higher-resolution meshes. Third, our method reduces the computational overhead during neural network updates by avoiding the multiplication of large Jacobian matrices associated with rendering during the backward pass. As shown in Table 1, our backward simulation is 2–3× faster than SHAC, measured on the same machine. Lastly, developing high-quality differentiable rendering software demands substantial engineering effort. In contrast, our method does not depend on such software, enabling easier integration into existing simulation ecosystems [Todorov et al., 2012, Xian et al., 2024], with the potential to handle multi-modal observation such as point clouds or LiDAR scans.

Table 1: Backward time for a single training episode.

	Cartpole	Hopper	Ant	Humanoid
Ours	0.11(s)	0.19(s)	0.21(s)	0.68(s)
SHAC	0.36(s)	0.51(s)	0.58(s)	1.38(s)

5 Related Work

Visual policy learning Techniques integrating learned image encoders [Finn et al., 2015, Mnih et al., 2015] have shown promising results in visual policy learning. Building on these approaches, algorithms such as Kostrikov et al. [2020], Yarats et al. [2021] improve performance through data augmentation, Laskin et al. [2020a,b], Stooke et al. [2021] leverage contrastive learning, and Hafner et al. [2019, 2023], Hansen et al. [2022] address the visual-control problem by learning world models for online planning. While these methods effectively tackle image-control challenges, they often require extensive environmental interaction and suffer from computational inefficiencies. In this work, we introduce a method that leverages differentiable simulation to reduce training time.

Policy learning with differentiable simulation Analytical policy gradient methods [Freeman et al., 2021, Qiao et al., 2021, Mora et al., 2021] have gained traction with the rise of differentiable simulation. Among them, SHAC [Xu et al., 2021] addresses noisy optimization via short-horizon rollouts and a value function, making it a core technique in many downstream robotics applications [Schwarke et al., 2024, Song et al., 2024]. Recent efforts have adapted APG to visual policy learning: Wiedemann et al. [2023] incorporates differentiable rendering, while Heeg et al. [2024] uses cropped vision features for quadrotor racing. Luo et al. [2024] propose a hierarchical design separating control and perception. However, these approaches remain task-specific and engineering-heavy. In contrast, our method generalizes across tasks and achieves higher computational efficiency than prior visual policy learning methods.

6 Conclusion

Our algorithm, D.Va, is a computationally efficient method for training visual policies utilizing differentiable simulation and first-order policy gradients. With this approach, we are able to train complex visual policies within hours using modest computational resources. We believe that this improvement in computational efficiency can unlock new possibilities for the robotics community, enabling practical end-to-end training of policies from raw observations. A key limitation of our

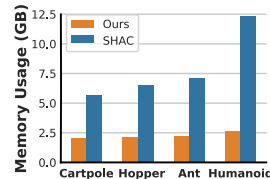


Figure 10: **Peak memory usage during training. Our method is 3–5× more memory efficient than SHAC.** Each task is run with 32 parallel environments and a short horizon length of 32.

method is that its success depends heavily on the quality and accuracy of the simulation environment. However, this limitation is shared by all baseline methods, as training directly in the real world is often impractical. Future research should focus on how to effectively transfer the success of training visual policies in simulation to real-world scenarios.

References

- Kevin Black, Noah Brown, Danny Driess, Adnan Esmail, Michael Equi, Chelsea Finn, Niccolo Fusai, Lachy Groom, Karol Hausman, Brian Ichter, Szymon Jakubczak, Tim Jones, Liyiming Ke, Sergey Levine, Adrian Li-Bell, Mohith Mothukuri, Suraj Nair, Karl Pertsch, Lucy Xiaoyang Shi, James Tanner, Quan Vuong, Anna Walling, Haohuan Wang, and Ury Zhilinsky. π_0 : A vision-language-action flow model for general robot control, 2024. URL <https://arxiv.org/abs/2410.24164>.
- Mariusz Bojarski, Davide Del Testa, Daniel Dworakowski, Bernhard Firner, Beat Flepp, Praseon Goyal, Lawrence D Jackel, Mathew Monfort, Urs Muller, Jiakai Zhang, et al. End to end learning for self-driving cars. *arXiv preprint arXiv:1604.07316*, 2016.
- Tao Chen, Megha Tippur, Siyang Wu, Vikash Kumar, Edward Adelson, and Pulkit Agrawal. Visual dexterity: In-hand reorientation of novel and complex object shapes. *Science Robotics*, 8(84): eadc9244, 2023.
- Cheng Chi, Zhenjia Xu, Siyuan Feng, Eric Cousineau, Yilun Du, Benjamin Burchfiel, Russ Tedrake, and Shuran Song. Diffusion policy: Visuomotor policy learning via action diffusion. *The International Journal of Robotics Research*, 2024.
- Chelsea Finn, Xin Yu Tan, Yan Duan, Trevor Darrell, Sergey Levine, and Pieter Abbeel. Learning visual feature spaces for robotic manipulation with deep spatial autoencoders. *arXiv preprint arXiv:1509.06113*, 25(2), 2015.
- C. Daniel Freeman, Erik Frey, Anton Raichuk, Sertan Girgin, Igor Mordatch, and Olivier Bachem. Brax - a differentiable physics engine for large scale rigid body simulation, 2021. URL <http://github.com/google/brax>.
- Tuomas Haarnoja, Aurick Zhou, Pieter Abbeel, and Sergey Levine. Soft actor-critic: Off-policy maximum entropy deep reinforcement learning with a stochastic actor. In *International conference on machine learning*, pages 1861–1870. Pmlr, 2018.
- Danijar Hafner, Timothy Lillicrap, Ian Fischer, Ruben Villegas, David Ha, Honglak Lee, and James Davidson. Learning latent dynamics for planning from pixels. In *International conference on machine learning*, pages 2555–2565. PMLR, 2019.
- Danijar Hafner, Jurgis Pasukonis, Jimmy Ba, and Timothy Lillicrap. Mastering diverse domains through world models. *arXiv preprint arXiv:2301.04104*, 2023.
- Nicklas Hansen, Xiaolong Wang, and Hao Su. Temporal difference learning for model predictive control. *arXiv preprint arXiv:2203.04955*, 2022.
- Johannes Heeg, Yunlong Song, and Davide Scaramuzza. Learning quadrotor control from visual features using differentiable simulation. *arXiv preprint arXiv:2410.15979*, 2024.
- Alex Kendall, Jeffrey Hawke, David Janz, Przemyslaw Mazur, Daniele Reda, John-Mark Allen, Vinh-Dieu Lam, Alex Bewley, and Amar Shah. Learning to drive in a day. In *2019 international conference on robotics and automation (ICRA)*, pages 8248–8254. IEEE, 2019.
- Ilya Kostrikov, Denis Yarats, and Rob Fergus. Image augmentation is all you need: Regularizing deep reinforcement learning from pixels. *arXiv preprint arXiv:2004.13649*, 2020.
- Michael Laskin, Aravind Srinivas, and Pieter Abbeel. Curl: Contrastive unsupervised representations for reinforcement learning. *Proceedings of the 37th International Conference on Machine Learning, Vienna, Austria, PMLR 119*, 2020a. arXiv:2004.04136.
- Misha Laskin, Kimin Lee, Adam Stooke, Lerrel Pinto, Pieter Abbeel, and Aravind Srinivas. Reinforcement learning with augmented data. *Advances in neural information processing systems*, 33: 19884–19895, 2020b.

- Timothy P Lillicrap, Jonathan J Hunt, Alexander Pritzel, Nicolas Heess, Tom Erez, Yuval Tassa, David Silver, and Daan Wierstra. Continuous control with deep reinforcement learning. *arXiv preprint arXiv:1509.02971*, 2015.
- Ruoshi Liu, Alper Canberk, Shuran Song, and Carl Vondrick. Differentiable robot rendering, 2024. URL <https://arxiv.org/abs/2410.13851>.
- Antonio Loquercio, Elia Kaufmann, René Ranftl, Matthias Müller, Vladlen Koltun, and Davide Scaramuzza. Learning high-speed flight in the wild. *Science Robotics*, 6(59):eabg5810, 2021.
- Jing Yuan Luo, Yunlong Song, Victor Klemm, Fan Shi, Davide Scaramuzza, and Marco Hutter. Residual policy learning for perceptive quadruped control using differentiable simulation, 2024. URL <https://arxiv.org/abs/2410.03076>.
- Luke Metz, C Daniel Freeman, Samuel S Schoenholz, and Tal Kachman. Gradients are not all you need. *arXiv preprint arXiv:2111.05803*, 2021.
- Volodymyr Mnih, Koray Kavukcuoglu, David Silver, Andrei A Rusu, Joel Veness, Marc G Bellemare, Alex Graves, Martin Riedmiller, Andreas K Fidjeland, Georg Ostrovski, et al. Human-level control through deep reinforcement learning. *nature*, 518(7540):529–533, 2015.
- Miguel Angel Zamora Mora, Momchil Peychev, Sehoon Ha, Martin Vechev, and Stelian Coros. Pods: Policy optimization via differentiable simulation. In *International Conference on Machine Learning*, pages 7805–7817. PMLR, 2021.
- Tongzhou Mu, Zhaoyang Li, Stanisław Strzelecki, Xiu Yuan, Yunchao Yao, Litian Liang, and Hao Su. When should we prefer state-to-visual dagger over visual reinforcement learning? In *Proceedings of the AAAI Conference on Artificial Intelligence*, 2025.
- Yi-Ling Qiao, Junbang Liang, Vladlen Koltun, and Ming C Lin. Efficient differentiable simulation of articulated bodies. In *International Conference on Machine Learning*, pages 8661–8671. PMLR, 2021.
- Nikhila Ravi, Jeremy Reizenstein, David Novotny, Taylor Gordon, Wan-Yen Lo, Justin Johnson, and Georgia Gkioxari. Accelerating 3d deep learning with pytorch3d. *arXiv:2007.08501*, 2020.
- Stéphane Ross, Geoffrey Gordon, and Drew Bagnell. A reduction of imitation learning and structured prediction to no-regret online learning. In *Proceedings of the fourteenth international conference on artificial intelligence and statistics*, pages 627–635. JMLR Workshop and Conference Proceedings, 2011.
- Clemens Schwarke, Victor Klemm, Jesus Tordesillas, Jean-Pierre Sleiman, and Marco Hutter. Learning quadrupedal locomotion via differentiable simulation. *arXiv preprint arXiv:2404.02887*, 2024.
- Yunlong Song, Sangbae Kim, and Davide Scaramuzza. Learning quadruped locomotion using differentiable simulation. *arXiv preprint arXiv:2403.14864*, 2024.
- Adam Stooke, Kimin Lee, Pieter Abbeel, and Michael Laskin. Decoupling representation learning from reinforcement learning. In *International conference on machine learning*, pages 9870–9879. PMLR, 2021.
- Hyung Ju Suh, Max Simchowitz, Kaiqing Zhang, and Russ Tedrake. Do differentiable simulators give better policy gradients? In *International Conference on Machine Learning*, pages 20668–20696. PMLR, 2022.
- Richard S Sutton, Andrew G Barto, et al. Introduction to reinforcement learning, vol. 135, 1998.
- Stone Tao, Fanbo Xiang, Arth Shukla, Yuzhe Qin, Xander Hinrichsen, Xiaodi Yuan, Chen Bao, Xinsong Lin, Yulin Liu, Tse kai Chan, Yuan Gao, Xuanlin Li, Tongzhou Mu, Nan Xiao, Arnab Gurha, Zhiao Huang, Roberto Calandra, Rui Chen, Shan Luo, and Hao Su. Maniskill3: Gpu parallelized robotics simulation and rendering for generalizable embodied ai. *arXiv preprint arXiv:2410.00425*, 2024.

- Emanuel Todorov, Tom Erez, and Yuval Tassa. Mujoco: A physics engine for model-based control. In *2012 IEEE/RSJ International Conference on Intelligent Robots and Systems*, pages 5026–5033. IEEE, 2012. doi: 10.1109/IROS.2012.6386109.
- Nina Wiedemann, Valentin Wüest, Antonio Loquercio, Matthias Müller, Dario Floreano, and Davide Scaramuzza. Training efficient controllers via analytic policy gradient. In *2023 International Conference on Robotics and Automation (ICRA)*. IEEE, 2023.
- Zhou Xian, Qiao Yiling, Xu Zhenjia, Wang Tsun-Hsuan, Chen Zhehuan, Zheng Juntian, Xiong Ziyang, Zhang Mingrui Wang Yian, Ma Pingchuan, Wang Yufei, and Dou Zhiyang. Genesis: A universal and generative physics engine for robotics and beyond, December 2024. URL <https://github.com/Genesis-Embodied-AI/Genesis>.
- Jie Xu, Viktor Makoviychuk, Yashraj Narang, Fabio Ramos, Wojciech Matusik, Animesh Garg, and Miles Macklin. Accelerated policy learning with parallel differentiable simulation. In *International Conference on Learning Representations*, 2021.
- Denis Yarats, Amy Zhang, Ilya Kostrikov, Brandon Amos, Joelle Pineau, and Rob Fergus. Improving sample efficiency in model-free reinforcement learning from images, 2020. URL <https://arxiv.org/abs/1910.01741>.
- Denis Yarats, Rob Fergus, Alessandro Lazaric, and Lerrel Pinto. Mastering visual continuous control: Improved data-augmented reinforcement learning. *arXiv preprint arXiv:2107.09645*, 2021.

Appendix

A Additional derivation

A.1 Derivative of analytical policy gradient separation

In this section, we provide a detailed derivation of how the analytical policy gradient $\nabla_{\theta} \mathcal{V}$ (1) can be decomposed into the decoupled policy gradient $\tilde{\nabla}_{\theta} \mathcal{V}$ (4) and control regularized term \mathcal{B} (5). We achieve this decomposition through pattern matching.

We begin with the decoupled policy gradient (4), which is obtained by taking the expectation over the gradient of individual trajectories. The gradient of each trajectory, in turn, is computed by summing the gradients of the temporal running rewards, as follows:

$$\tilde{\nabla}_{\theta} \mathcal{J}(s_0, \theta, \mathcal{E}) = \sum_{t=0}^T \tilde{\nabla}_{\theta} r_t. \quad (11)$$

The gradient of the running reward, $\tilde{\nabla}_{\theta} r_t$, is composed of two partial derivatives. First, the immediate reward r_t is directly influenced by the action taken at time step t , denoted \mathbf{a}_t . This yields the partial derivative term:

$$\frac{\partial r_t}{\partial \mathbf{a}_t} \frac{\partial \mathbf{a}_t}{\partial \theta}.$$

Second, the reward r_t also depends on the state s_t , which itself depends on the previous state s_{t-1} and action \mathbf{a}_{t-1} . In the decoupled formulation, this dependency propagates backward through time, leading to a recursive gradient computation. Specifically, the second term is

$$\frac{\partial r_t}{\partial s_t} \frac{ds_t}{d\theta},$$

where the derivative $\frac{ds_t}{d\theta}$ is given recursively by: $\frac{ds_t}{d\theta} = \frac{\partial s_t}{\partial s_{t-1}} \frac{ds_{t-1}}{d\theta} + \frac{\partial s_t}{\partial \mathbf{a}_{t-1}} \frac{\partial \mathbf{a}_{t-1}}{\partial \theta}$. Altogether, we have

$$\tilde{\nabla}_{\theta} r_t = \frac{\partial r_t}{\partial \mathbf{a}_t} \frac{\partial \mathbf{a}_t}{\partial \theta} + \frac{\partial r_t}{\partial s_t} \frac{ds_t}{d\theta}. \quad (12)$$

Figure 11 illustrates a typical backward flow on decoupled policy gradient starting with the reward r_2 .

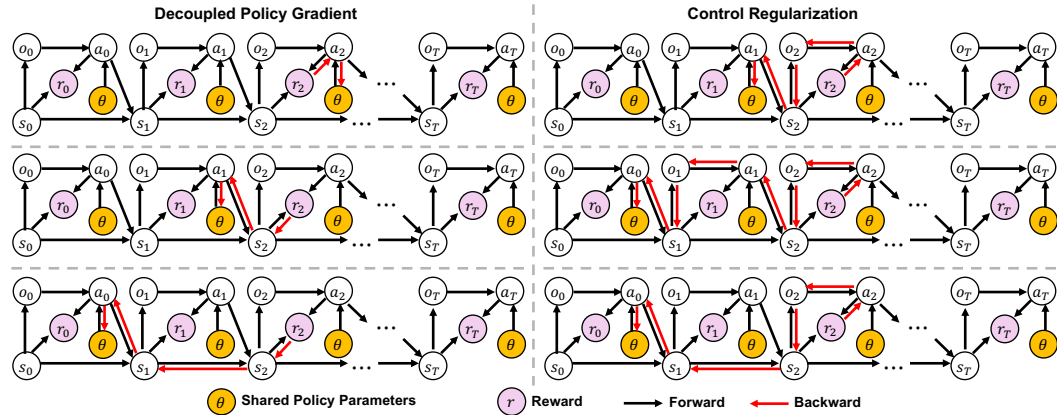


Figure 11: **Backward gradient start with r_2 .** Left: the backward gradient flow on the decoupled policy gradient. Right: the backward flow on control regularization. Each subplot in the row starts from the reward node r_2 and traces backward along the computation graph until it reaches the policy parameters θ , illustrating a partial contribution to the total derivative.

We now examine how the control regularization term (5) is formulated. Following the structure illustrated in Figure 11, the control regularization is constructed by summing a series of terms of the form:

$$\frac{\partial r_t}{\partial \mathbf{a}_t} \frac{\partial \mathbf{a}_t}{\partial \mathbf{o}_t} \frac{d\mathbf{o}_t}{ds_t} \frac{ds_t}{d\theta}.$$

Here, the total derivative $\frac{ds_t}{d\theta}$ can be computed recursively as follows:

$$\frac{ds_t}{d\theta} = \frac{\partial s_t}{\partial \mathbf{a}_{t-1}} \left(\frac{\partial \mathbf{a}_{t-1}}{\partial \theta} + \frac{\partial \mathbf{a}_{t-1}}{\partial \mathbf{o}_{t-1}} \frac{d\mathbf{o}_{t-1}}{ds_{t-1}} \frac{ds_{t-1}}{d\theta} \right) + \frac{\partial s_t}{\partial s_{t-1}} \frac{ds_{t-1}}{d\theta}. \quad (13)$$

Altogether, the control regularization term is given in Eq. (5). Thus, the full analytical policy gradient is the sum of the decoupled policy gradient and the control regularization term:

$$\nabla_{\theta} \mathcal{V} = \tilde{\nabla}_{\theta} \mathcal{V} + \mathcal{B}. \quad (14)$$

B Additional implementation details

B.1 D.VA algorithm

Critic Learning Our critic training follows SHAC, minimizing the mean squared error over collected trajectories:

$$\mathcal{L}_{\phi} = \mathbb{E}_{\mathbf{s} \in \{\tau^{(i)}\}} \left[\|V_{\phi}(s) - \tilde{V}(\mathbf{s})\|_2^2 \right], \quad (15)$$

where

$$\tilde{V}(\mathbf{s}_t) = (1 - \lambda) \left(\sum_{k=1}^{h-t-1} \lambda^{k-1} G_t^k \right) + \lambda^{h-t-1} G_t^{h-t}, \quad (16)$$

is the estimated value function and is treated as a constant target during critic learning. Here, $G_t^k = \left(\sum_{l=0}^{k-1} \gamma^l R(\mathbf{s}_{t+l}, \mathbf{a}_{t+l}) \right) + \gamma^k V_{\phi'}(\mathbf{s}_{t+k})$ represents the k -step return from time t , and $V_{\phi'}$ is a delayed critic function used to stabilize the training process [Mnih et al., 2015].

Full algorithm Below, we summarize our Decoupled Visual-Based Analytical Policy Gradient (D.VA) algorithm.

Algorithm 1: D.VA (Decoupled Visual Based Analytical Policy Gradient)

Function Rollout()
Initialize N initial states \mathbf{s}_0 .
for $t = 0$ to $h - 1$ **do**
 with torch.no_grad():
 compute pixel images $\mathbf{o}_t = g(\mathbf{s}_t)$.
 Sample actions $a_t \sim \pi_{\theta}(\mathbf{o}_t)$, simulate and compute rewards r_t and next states \mathbf{s}_{t+1} .
end for
Collect N trajectories $\tau = \{(\mathbf{s}_t, a_t, r_t)\}_{t=0}^{h-1}$ and compute actor loss \mathcal{L}_{θ} via Eq. (3).
Return $\tau, \mathcal{L}_{\theta}$
Function Main()
Initialize $\pi_{\theta}, V_{\phi}, V_{\phi'} \leftarrow V_{\phi}$
for $epoch = 1$ to M **do**
 Generate N short-horizon trajectories τ and compute actor loss \mathcal{L}_{θ} by calling Rollout().
 Compute decoupled policy gradient $\tilde{\nabla}_{\theta} \mathcal{V}$ and update π_{θ} with Adam.
 Fit value function V_{ϕ} via critic loss (15) and update delayed target $V_{\phi'} \leftarrow \alpha V_{\phi'} + (1 - \alpha) V_{\phi}$.
end for

B.2 Differentiable Rendering

In this section, we present the construction of our differentiable renderer, designed to facilitate end-to-end training.

Given a state vector $\mathbf{s} = [\mathbf{q}^{\top}, \dot{\mathbf{q}}^{\top}]^{\top}$, where $\mathbf{q} \in \mathbb{R}^n$ represents joint positions and $\dot{\mathbf{q}}$ denotes joint velocities, which have dimension $m - 1$ or m depending on the presence of quaternions. We compute m homogeneous transformations \mathbf{T} for forward kinematics. These transformations encode the rotation and translation from the world frame to each joint frame and are used to transform geometry meshes defined in local joint frames to assemble the full robot mesh. Lighting and camera poses are also updated using these transformations to set up the full scene. Finally, we render the scene using PyTorch3D via rasterization. Figure 12 summarizes the whole process.

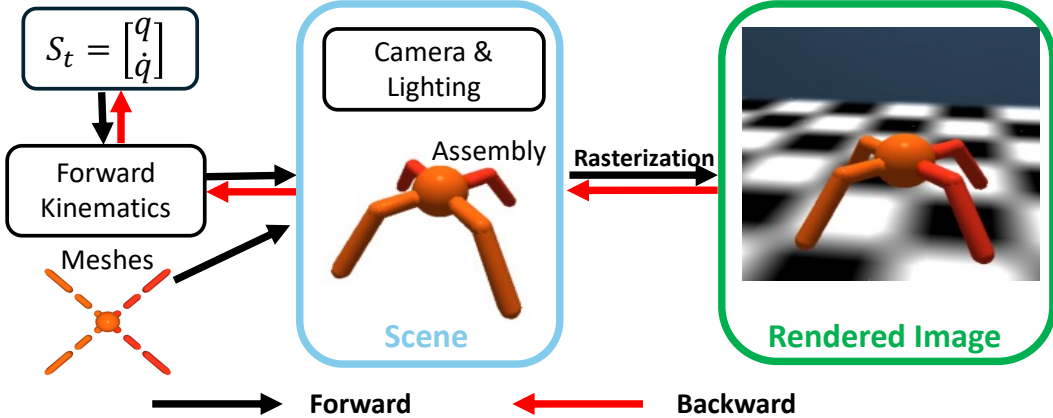


Figure 12: Diagram for differentiable rendering

C Hyperparameters

In this section, we describe our hyperparameter tuning process and share additional insights gained during experimentation. Detailed hyperparameter values are provided at the end.

C.1 How we tune hyperparameters

For all baseline methods, we initialized hyperparameters using values reported in the original papers. We then identified the most sensitive hyperparameters and tuned them sequentially. Additional attention is given to those hyperparameters emphasized in the original works. This process involved over 500 experiments, with some trials manually terminated early when it became evident that the chosen hyperparameters were suboptimal. In contrast, we did not apply additional tuning to our proposed method, as the combination of hyperparameters from state-based SHAC and the encoder architecture from DrQV2 already yielded strong performance.

We summarize our key findings from the tuning process and present the final hyperparameter values used in the following sections.

C.2 Key findings and experimental settings

DrQ-v2 We implement DrQ-v2 with parallelized forward simulation to improve wall-clock time efficiency. During each training episode, we concurrently collect new samples using the current policy across multiple parallel environments. After data collection, we perform several update steps on the Q-functions using the data from the replay buffer. The forward pass accounts for only a small portion of the total training time with parallelization, as shown in Figure 5. The majority of computation time is instead dedicated to updating the agent’s neural network, i.e., Q-function and Actor. We found that the ratio between agent update steps and new sample collection plays a critical role in achieving good performance. While performing multiple agent updates per environment step can improve sample efficiency, it may negatively impact wall-clock time performance. In addition, we observe that excessive updates can harm final policy performance due to outdated data from the replay buffer. Therefore, we carefully tune both the number of parallel environments and the number of updates per training episode, aiming to maximize wall-clock efficiency and final return. The hyperparameters used in our experiments are listed in Table 2. The primary difference from the original DrQ-v2 setup is that we increase both the number of parallel environments and the number of agent updates per step, while the ratio is kept the same. Unless otherwise noted, the same parameters are used across all four tasks. We kept neural architecture identical to that used in the original paper and summarize in Table 3 and 4:

CURL We also apply parallelized forward simulation to CURL to accelerate training. Similar to DrQ-v2, the update frequency plays a critical role in achieving strong performance. We tune the number of parallel environments to optimize wall-clock efficiency within the available GPU memory budget. The training parameters used for CURL are listed in Table 5. Notably, CURL uses a similar

Table 2: DrQ-v2 training parameters

Parameter name	Value
Number of parallel environments	32; 16 for Cartpole
Number of agent updates	16; 8 for Cartpole
Replay buffer capacity	10^6
Action repeat	2
Mini-batch size	256
N-step returns	3
Discount factor γ	0.99
Learning rate	10^{-4} ; (8×10^{-5} for Humanoid)
Critic Q-function soft-update rate	0.01
Exploration stddev. clip	0.3
Exploration stddev. schedule	<code>linear(1.0, 0.1, 500000)</code> ; <code>linear(1.0, 0.1, 2000000)</code> for humanoid

Table 3: DrQV2 encoder architectures

Parameter name	Value
Input image size (height \times width)	84×84
Convolution kernel size	3, 3, 3, 3
Convolution output channel size	32, 32, 32, 32
Convolution activation function	Relu

Table 4: DrQ-v2 actor-critic architecture

Task name	Trunk size	Policy network	Critic network
Cartpole	50	[1024, 1024]	[1024, 1024]
Hopper	50	[1024, 1024]	[1024, 1024]
Ant	50	[1024, 1024]	[1024, 1024]
Humanoid	100	[1024, 1024]	[1024, 1024]

architecture to DrQ-v2 (see Table 3, and 4); both are adopted from Yarats et al. [2020]. To ensure a fair comparison, we use the same architecture for both algorithms, avoiding confounding factors introduced by architectural differences.

DreamerV3 Our implementation of DreamerV3 builds upon the open-source repository available at <https://github.com/NM512/dreamerv3-torch>. We parallelized the environment stepping in our implementation; however, we observed that this parallelization has minimal impact on performance—consistent with the findings reported by the author of the repository. Additionally, DreamerV3 is a memory-intensive algorithm, which limits the degree of parallelism we can apply. The detailed hyperparameters for training are mostly kept the same as those used in Hafner et al. [2023] and listed in Table 6. The neural architecture remains unchanged from the Hafner et al. [2023].

D.Va (Ours) Architecture details: Stacked images are first processed by an encoder to generate a hidden state. The encoder is a 4-layer convolutional network, identical to that used in DrQ-v2 (Table 3). The hidden state is then passed to the actor network to generate actions. The actor network consists of a trunk network and a policy network, following the design of DrQ-v2. The trunk network is a single linear layer followed by layer normalization. The policy and critic network is adopted from the state-based SHAC: MLP network with ELU activation and layer normalization. The detailed network architectures are provided in Table 7.

Table 5: CURL training parameters

Parameter name	Value
Number of parallel environments	16
Number of agent updates	8
Replay buffer capacity	10^5
Action repeat	2
Batch size	32
Discount factor γ	0.99
Actor learning rate	10^{-3}
Critic learning rate	10^{-3}
Adam (β_1, β_2) for actor and critic	(0.9, 0.99)
Q-function soft-update rate	0.01
Initial temperature	0.1
Temperature learning rate	10^{-4}
Adam (β_1, β_2) for temperature	(0.5, 0.99)

Table 6: DreamerV3 training parameters

Parameter name	Value
Image size (height \times width)	(64 \times 64)
Number of parallel environments	4
Batch size	16
Batch length	64
Train ratio	512
Action repeat	2
Replay buffer capacity	10^6
Action repeat	2
Discount factor γ	0.997
Discount lambda λ	0.95
Actor learning rate	3×10^{-5}
Critic learning rate	3×10^{-5}
Actor-critic adam epsilon	10^{-5}
World model learning rate	10^{-4}
World model adam epsilon	10^{-8}
Critic EMA decay	0.98
Reconstruction loss scale	1.0
Dynamics loss scale	0.5
Representation loss scale	0.1
Actor entropy scale	3×10^{-4}
Return normalization decay	0.99

Table 7: D.Va actor-critic architecture

Task name	Trunk size	Policy network	Critic network
Cartpole	64	[64, 64]	[64, 64]
Hopper	128	[128, 64, 32]	[64, 64]
Ant	128	[128, 64, 32]	[64, 64]
Humanoid	256	[256, 128]	[128, 128]

For training, we apply a linear decay schedule to adjust the learning rate over episodes, with specific hyperparameters provided in Table 8.

Table 8: D.Va training parameters

Parameter name	Cartpole	Hopper	Ant	Humanoid
Short horizon length h	32			
Number of parallel environments N	64			
Actor learning rate	0.002			
Critic learning rate	0.0002		0.002	0.0005
Target value network α	0.2			0.995
Discount factor γ	0.99			
Value estimation λ	0.95			
Adam (β_1, β_2)	(0.7, 0.95)			
Number of critic training iterations	16			
Number of critic training minibatches	4			

State-to-visual Distillation The architecture is kept identical to that used for D.Va, which can be found in Table 3 and 7. As described earlier, the architecture is constructed by simply concatenating the DrQv2 encoder with the SHAC state-based architecture, ideally, no method is unfairly favored. The hyperparameters are tuned following the guidelines of Mu et al. [2025]. We found that, to make State-to-Visual Distillation work effectively, the most critical factor is the data collection strategy and the frequency of network updates, consistent with the findings reported in Mu et al. [2025]. Specifically, we collect data in a SHAC-style manner: instead of executing long, continuous trajectories, we roll out short-horizon segments that resume from the endpoint of the previous rollout. Notably, this implementation is the same as that used in Mu et al. [2025]. The detail parameters are listed in Table 9

Table 9: State-to-visual Distillation training parameters

Parameter name	Value
Short horizon length h	32
Number of parallel environments N	64
Learning rate	0.002
Adam (β_1, β_2)	(0.7, 0.95)
Batch size	128
Early stop threshold	0.1
Maximum reply buffer size	10^5

SHAC with differentiable rendering The neural architecture is kept identical to ours and is detailed in Table 3 and Table 7. For 3D tasks such as Ant and Humanoid, we observed that the gradient norm quickly diverges to infinity as the horizon length h increases. To address this, we use an even smaller horizon length compared to the one used for training state-based SHAC. The number of parallel environments is also reduced due to GPU memory constraints. The specific parameter values are provided in Table 10.

D Additional Experiment

D.1 Compare DPG to SHAC on state space

We provide additional experiments to validate using decoupled policy gradient is enough to gain good performance in many scenarios. Here, we conduct on state space, with a single line change on the original SHAC code: `actions = actor(obs)` to `actions = actor(obs.detach())`. We kept all hyperparameters identical to those reported in SHAC. Figure 13 compares the training performance of the SHAC with full analytical policy gradient 1 to our decoupled policy gradient 4. We find that

Table 10: Visual-SHAC training parameters

Parameter name	Cartpole	Hopper	Ant	Humanoid
Short horizon length h	32	32	8	32
Number of parallel environments N	64	64	32	32
Critic learning rate	0.0002		0.002	0.0005
Target value network α	0.2			0.995
Actor learning rate	0.002			
Discount factor γ	0.99			
Value estimation λ	0.95			
Adam (β_1, β_2)	(0.7, 0.95)			
Number of critic training iterations	16			
Number of critic training minibatches	4			

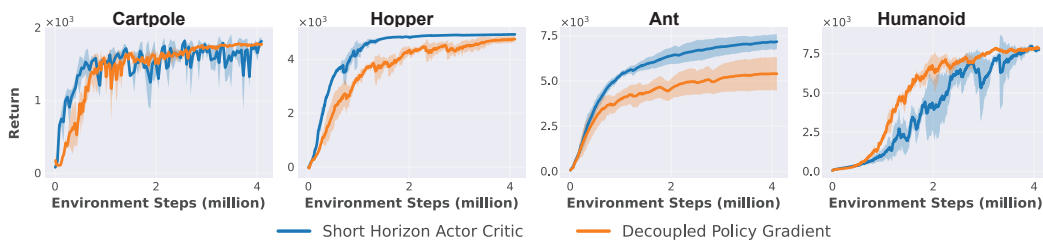


Figure 13: **Comparison between DPG and SHAC on state space:** Experiments are conducted with low-dimensional state observations and results are averaged over five random seeds. All hyperparameters are kept identical to those used in the original SHAC. DPG still achieves comparable results in the settings that favor SHAC.

the decoupled policy gradient achieves performance comparable to SHAC on low-dimensional state spaces, even under settings that favor SHAC.

E Setup

E.1 Tasks Descriptions

We select four classical RL tasks across different complexity levels. The camera views are similar to those used in Yarats et al. [2021], as illustrated in Figure 14. Except for Cartpole, where the camera is fixed to the world frame, all other cameras track the position of the robot’s base joint. The motion of Cartpole and Hopper is constrained to 2D, whereas Ant and Humanoid are free to move in 3D space. The body of the Ant may block the view of some of its legs due to the side-view camera setup, making the environment partially observable. In contrast, the joints in all other environments remain visible from the camera regardless of posture, resulting in fully observable settings.

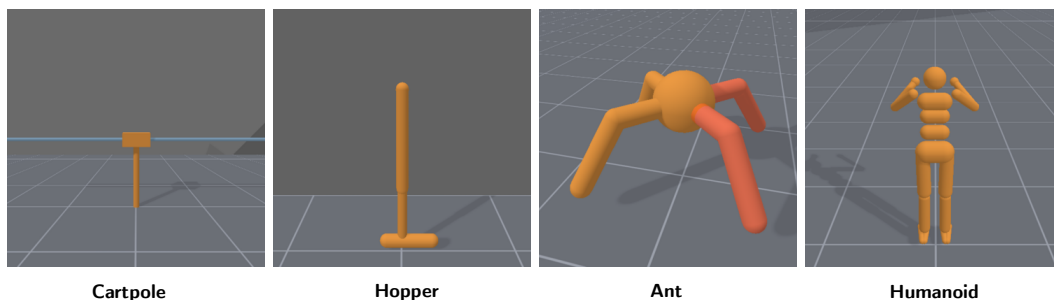


Figure 14: Camera views of each environment in ManiskillV3

The reward functions are identical to those used in the SHAC paper, except for the Cartpole system, where we add a health score to prevent the cart from moving off-screen. The details are summarized as follows:

Cartpole: The running rewards are defined as

$$R: = 10 - \theta^2 - 0.1\dot{\theta}^2 - 0.05x^2 - 0.1\dot{x}^2, \quad (17)$$

where θ , x denote the angle of pole from upright position and position of cart; and $\dot{\theta}$, \dot{x} are the angular and linear velocity respectively. The total trajectory length is 240, and early termination is triggered when Cartpole is outside the camera views, i.e., $|x| \geq 2.5$.

Hopper: The running rewards are defined as

$$R: = v_x - \left(\frac{\theta}{30^\circ}\right)^2 + R_{\text{height}} - 0.1\|\mathbf{a}\|, \quad (18)$$

where v_x is the forward velocity, θ is the orientation of base joint and

$$R_{\text{height}} = \begin{cases} -200\Delta_h^2, & \Delta_h \leq 0 \\ \Delta_h, & \Delta_h > 0 \end{cases}; \quad \Delta_h = \text{clip}(h + 0.3, -1, 0.3), \quad (19)$$

is designed to penalize the low height state. The total trajectory length is 1000, and early termination is triggered when the height of the hopper is lower than -0.45m.

Ant: The running rewards are defined as

$$R: = v_x + 0.1R_{\text{up}} + R_{\text{heading}} + p_z - 0.27, \quad (20)$$

where v_x is forward velocity, R_{up} , R_{heading} is the projection of base orientation in upright and forward direction, encouraging the agent to be vertically stable and run straightforward, p_z is the height of the base. The total trajectory length is 1000, and early termination is triggered when the height of the ant is lower than 0.27m.

Humanoid: The running rewards are defined as

$$R: = v_x + 0.1R_{\text{up}} + R_{\text{heading}} + R_{\text{height}} - 0.002\|\mathbf{a}\|, \quad (21)$$

where v_x is forward velocity, R_{up} , R_{heading} is the projection of base orientation in the upright and forward direction, and

$$R_{\text{height}} = \begin{cases} -200\Delta_h^2, & \Delta_h \leq 0 \\ \Delta_h, & \Delta_h > 0 \end{cases}; \quad \Delta_h = \text{clip}(h - 0.84, -1, 0.1). \quad (22)$$

The total trajectory length is 1000, and early termination is triggered when the height of the torso is lower than 0.74m.

E.2 Simulation

We use the same differentiable simulation framework proposed in SHAC as the underlying dynamics model. For the three benchmark RL methods and the state-to-visual tasks, we employ ManiSkill-V3 [Tao et al., 2024] for rendering. In contrast, for visual-SHAC, we implement a custom differentiable rendering pipeline using PyTorch3D, as detailed in Appendix B.2. All software components are GPU-accelerated and parallelized. We evaluate our method under both rendering pipelines. To ensure a fair comparison, all experiments presented in Section 4 are conducted using the same rendering setup across different methods. We find the ManiSkill implementation to be fairly efficient—approximately $3\times$ faster than our differentiable rendering pipeline—and therefore, we use differentiable rendering only when necessary. However, aside from the difference in forward rendering speed, we find that the final return and sample efficiency of our method remain similar across both rendering pipelines.

E.3 Hardware

All experiments are conducted on a single NVIDIA GeForce RTX 4080 GPU (16GB) with an Intel Xeon W5-2445 CPU and 256GB RAM. Unlike the case of simulating dynamics alone—where tens of thousands of environments can be parallelized at once—heterogeneous rendering requires significantly more memory. As a result, our hyperparameter tuning is carefully constrained to stay within the available memory budget.